

Differential charge radii: self-consistency and proton-neutron interaction effects

U. C. Perera¹ and A. V. Afanasjev¹

¹*Department of Physics and Astronomy, Mississippi State University, MS 39762*

(Dated: March 20, 2024)

The analysis of self-consistency and proton-neutron interaction effects in the buildup of differential charge radii has been carried out in covariant density functional theoretical calculations without pairing interaction. Two configurations of the ^{218}Pb nucleus, generated by the occupation of the neutron $1i_{11/2}$ and $2g_{9/2}$ subshells, are compared with the ground state configuration in ^{208}Pb . The interaction of added neutron(s) and the protons forming the $Z = 82$ proton core is responsible for a major contribution to the buildup of differential charge radii. It depends on the overlaps of proton and neutron wave functions and leads to a redistribution of single-particle density of occupied proton states which in turn modifies the charge radii. Self-consistency effects affecting the shape of proton potential, total proton densities and the energies of the single-particle proton states provide only secondary contribution to differential charge radii. The buildup of differential charge radii is a combination of single-particle and collective phenomena. The former is due to proton-neutron interaction, the impact of which is state dependent, and the latter reflects the fact that all occupied proton single-particle states contribute to this process. The neglect of either one of these aspects of the process by ignoring proton-neutron interaction and self-consistency effects as it is done in macroscopic+microscopic approach or by introducing the core as in spherical shell model introduces uncontrollable errors and restricts the applicability of such approaches to the description of differential charge radii. The analysis also indicates that both the Coriolis interaction in odd and odd-odd deformed nuclei and the residual interaction between unpaired proton and neutron in odd-odd nuclei could affect the odd-even staggering in charge radii if their impact on the wave function of the ground state of these nuclei is appreciable.

I. INTRODUCTION

Charge radii are among the most fundamental properties of atomic nuclei and during the last decade there was a significant increase in experimental and theoretical studies of this physical observable. The experimental results were reviewed in Refs. [1, 2] and recent experimental investigations were summarized in the introduction of Ref. [3]. The introduction to the latter publication provides also the overview of theoretical efforts. Theoretical calculations within different density functional theories (DFTs) provide a quite accurate global description of experimental charge radii presented in the compilation of Ref. [1]: the rms deviations of calculated charge radii r_{ch} from experimental ones are at the level of ≈ 0.03 fm [4] which corresponds to high average precision of 0.625% in the prediction of charge radii (see Ref. [3]).

The changes of the charge radii within the isotopic chain are measured with high precision using laser spectroscopy (see Refs. [1, 2]). Thus, the differential mean-square (ms) charge radii (see Eq. (3) below for definition), measured with high precision within the isotopic chains, become an important quantity. They have been studied within *ab initio* approaches (see, for example, Refs. [5, 6]), non-relativistic DFTs based on zero range Skyrme forces (see Refs. [7–10]), Fayans functional (see Refs. [11–13]) and finite range Gogny forces (see Refs. [5, 14]), non-relativistic Hartree-Fock-Bogoliubov (HFB) approach with a finite-range Yukawa interaction [15–17] and covariant density functional theory (CDFT) (see Refs. [3, 10, 18–20]).

Different aspects of the buildup of differential charge

radii within the isotopic chain with increasing neutron number have been investigated in these papers. In particular, it was found that the evolution of the charge radii within the isotopic chain with increasing neutron number is defined by the pull on the proton states generated by neutrons gradually added to the nuclear system [3, 8, 21, 22]. The most investigated case here is the kink in charge radii at $N = 126$ and the evolution of charge radii above $N = 126$ in the Pb isotopic chain. The pattern of these effects critically depends on the occupation of the $2g_{9/2}$ and $1i_{11/2}$ orbitals, on their relative energies, and on how close they are in energy [3, 8, 21]: the kink is generated only when neutron $1i_{11/2}$ orbitals are substantially occupied in the nuclei with $N > 126$.

Ref. [21] provided a hint on microscopic origin of this difference by revealing that it is traced back to the nodal structure of these two orbitals ($n = 1$ for $1i_{11/2}$ and $n = 2$ for $2g_{9/2}$, where n stands for principal quantum number) and the overlap of their wavefunctions with those of the proton states. However, as follows from the present study the interpretation of the pull of these neutron states on proton orbitals via the symmetry energy does not corresponds to real physical situation since it is related to proton-neutron interaction. The detailed global analysis of the impact of the occupation of neutron single-particle orbitals in the vicinity of spherical neutron shell closures generalized the results of Ref. [21] to whole nuclear chart (see discussion of Fig. 32 in Ref. [3]). It revealed strong correlations between the principal quantum number n of the single neutron orbital occupied above the neutron shell closure and the impact of the occupation of this orbital on differential charge radii: in a given isotopic chain

the largest impact on differential charge radii is provided by the occupation of the neutron orbital with the lowest n . As a consequence, a significant occupation of the $n = 1$ neutron subshell above the neutron shell closure is required for a creation of the kink in differential charge radii at this closure (see Ref. [3]).

Despite all these studies, there are the aspects of the process of the buildup of differential charge radii which are not completely understood on microscopic level and which have not been discussed in the literature. Thus, the goal of the present paper is to fill these gaps in our knowledge and to perform detailed studies of the impact of self-consistency effects and the interaction between neutron(s) added to a reference nucleus and the protons forming the proton subsystem on the buildup of differential charge radii. Of particular interest is the balance of these two types of contributions and the microscopic mechanisms affecting the changes of charge radii in the isotopic chain with increasing neutron number. The results of these studies will also allow to answer the question of the applicability of different theoretical frameworks to the description of differential charge radii and potential contributing factors to odd-even staggering in charge radii.

The paper is organized as follows. Sec. II provides a brief outline of theoretical formalism and the discussion of physical observables under study. The impact of self-consistency and proton-neutron interaction effects on differential charge radii is discussed in Sec. III. Sec. IV is dedicated to general observations following from this study. Finally, Sec. V summarizes the results of our paper.

II. THEORETICAL FORMALISM AND PHYSICAL OBSERVABLES

Theoretical calculations have been performed within the framework of covariant density functional theory (CDFT) [23] employing the modified version of the computer code restricted to spherical symmetry used in Ref. [24]. Since the details of the CDFT framework are widely available (see, for example, Ref. [23]), we focus on the physical quantities of the interest. The pairing correlations are neglected in the calculations in order to better understand the underlying physical mechanisms. The calculations are performed with the NL3* covariant energy density functional (CEDF) [25]. Its global performance in the description of the masses and charge radii is well documented (see Refs. [3, 4]). It was also recently used in the study of bubble nuclei (see Ref. [26]) the results of which have substantial overlap with some aspects of the present study; this is one of main reasons for the selection of this functional. Note that it is verified that main conclusions obtained in the present paper do not depend on the selection of the functional.

In order to better apprehend the role of self-consistency effects on differential charge radii we consider ground

state configuration in ^{208}Pb and two configurations of the ^{218}Pb nucleus labeled below as "Conf-1 $i_{11/2}$ " and "Conf-2 $g_{9/2}$ ". In these configurations of ^{218}Pb , ten neutrons outside the ^{208}Pb core are located in the $1i_{11/2}$ and $2g_{9/2}$ spherical subshells, respectively. We selected ^{218}Pb in order to maximize the effect of the addition of neutrons in a given spherical subshell on proton charge radii¹. Note that the maximum number of neutrons which can be put into the $2g_{9/2}$ and $1i_{11/2}$ spherical subshells is 10 and 12, respectively. Thus, the selection of ^{218}Pb nucleus corresponds to full filling of the $2g_{9/2}$ neutron subshell and almost (two neutrons short) full filling of the $1i_{11/2}$ neutron subshell.

The charge radii are defined as

$$r_{ch} = \sqrt{\langle r^2 \rangle_p} + 0.64 \text{ fm} \quad (1)$$

where the mean square proton point radius is given by

$$\langle r^2 \rangle_p = \frac{\int r^2 \rho_{tot}^p(\vec{r}) d^3r}{\int \rho_{tot}^p(\vec{r}) d^3r} \quad (2)$$

and the factor 0.64 accounts for the finite-size effects of the proton². Then differential mean-square charge radius is given by³

$$\begin{aligned} \delta \langle r^2 \rangle_p^{N,N'} &= \langle r^2 \rangle_p(N) - \langle r^2 \rangle_p(N') = \\ &= r_{ch}^2(N) - r_{ch}^2(N'). \end{aligned} \quad (3)$$

Note that N' is the neutron number of the reference nucleus (^{208}Pb in this paper).

The total nucleonic density $\rho_{tot}(r)$ in a given subsystem (proton or neutron) is built from the contributions of individual particles as follows:

$$\rho_{tot}(r) = \sum_i m_i \rho_i^{sp}(r), \quad (4)$$

where m_i is the multiplicity of the occupation of the i -th subshell [$m_i = (2j_i + 1)$] for a fully occupied subshell with

¹ One can definitely consider the $1i_{11/2}$ and $2g_{9/2}$ configurations in odd- A ^{209}Pb nucleus and this will completely justify the neglect of pairing which collapses because of the blocking of odd neutron. However, this will not change the results and conclusions of the paper.

² Small contributions to the charge radii originating from the electric neutron form factor and electromagnetic spin-orbit coupling [27, 28] are neglected in the NL3* functional (as well as in the fitting protocols of all existing CEDFs). More precise expressions for charge radii in CDFT are available but their use would require the refit of the CEDFs (see Refs. [29, 30] and discussion in Sec. VIII of Ref. [3]). However, this neglect is not critical since spin-orbit contribution to charge radii decreases with increasing the mass of nuclei [29, 31] and its contribution to differential charge radii of the Pb isotopes is expected to be negligible [31].

³ This quantity is frequently written as a function of mass number A . However, we prefer to define it as a function of neutron number N since this allows to see the behavior of the $\delta \langle r^2 \rangle_p^{N,N'}$ curves at neutron shell closures.

angular momentum j_i] and $\rho_i^{sp}(r)$ is the density of the single-particle state belonging to the i -th subshell with the normalization

$$\int \rho_i^{sp}(\vec{r})d^3r = 4\pi \int r^2 \rho_i^{sp}(r)dr = 1.0. \quad (5)$$

Taking into account that $\int \rho_{tot}^p(\vec{r})d^3r = Z$ and that all proton subshells below the $Z = 82$ shell gap are fully occupied in the proton subsystem of the Pb isotopes, Eq. (2) can be rewritten as

$$\langle r^2 \rangle_p = \frac{1}{Z} \sum_i (2j_i + 1) \langle r^2 \rangle_i^p \quad (6)$$

where

$$\langle r^2 \rangle_i^p = \int r^2 \rho_i^p(\vec{r})d^3r \quad (7)$$

is the proton mean square radius of the single-particle state belonging to the i -th subshell. As a consequence, the differential charge radius of two isotopes can be re-defined as

$$\delta \langle r^2 \rangle_p^{N,N'} = \frac{1}{Z} \sum_i (2j_i + 1) [\langle r^2 \rangle_i^p(N) - \langle r^2 \rangle_i^p(N')] \quad (8)$$

and its magnitude could be traced back to the modifications in proton mean square radius of the single-particle states generated by the transition from the nucleus with neutron number N' to the nucleus with N . The quantity

$$\Delta \langle r^2 \rangle_i^{N,N'} = \langle r^2 \rangle_i^p(N) - \langle r^2 \rangle_i^p(N') \quad (9)$$

is denoted here as differential single-particle proton radius of the single-particle state belonging to the i -th proton subshell.

Note that for simplicity of the discussion of the role of the single-particle states we consider also single-particle rms radii r_i^p of the proton states defined as

$$r_i^p = \sqrt{\langle r^2 \rangle_i^p}. \quad (10)$$

The proton ($i = \pi$) and neutron ($i = \nu$) nucleonic potentials are defined in the CDFT as follows:

$$V_\pi = V + S + V_{Coul}, \quad (11)$$

$$V_\nu = V + S, \quad (12)$$

where scalar potential is given by

$$S(r) = g_\sigma \sigma(r), \quad (13)$$

meson defined part of the vector potential is written as

$$V(r) = g_\omega \omega_0(r) + g_\rho \tau_3 \rho_0(r), \quad (14)$$

and

$$V_{Coul}(r) = eA_0(r) \quad (15)$$

is the Coulomb potential.

III. THE ROLE OF SELF-CONSISTENCY AND PROTON-NEUTRON INTERACTION EFFECTS

A. Nucleonic potentials and densities

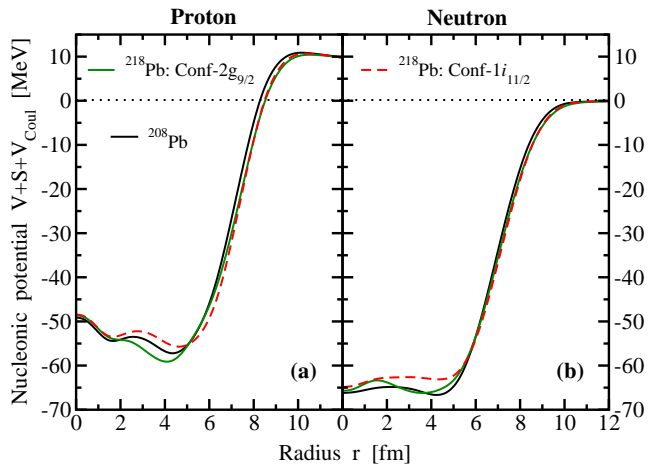


FIG. 1. Proton and neutron nucleonic potentials in the configurations under study. Dotted horizontal line shows zero energy threshold. Note that $V_{Coul} = 0$ in the panel (b).

To better understand the impact of the occupation of different neutron spherical subshells on charge radii of the $Z = 82$ core we first consider how nucleonic potentials and densities change on transition from the ^{208}Pb nucleus to the "Conf- $1i_{11/2}$ " and "Conf- $2g_{9/2}$ " configurations in the ^{218}Pb nucleus.

Proton and neutron nucleonic potentials of the configurations under study are shown in Fig. 1. The addition of ten neutrons to the ^{208}Pb core only slightly increases the radius of neutron potential and the shapes of neutron potentials of the "Conf- $1i_{11/2}$ " and "Conf- $2g_{9/2}$ " configurations in ^{218}Pb are almost identical in the energy range between -60 MeV and 0 MeV [see Fig. 1(b)]. The largest changes are seen at the bottom of the neutron potentials which affects mostly deep lying neutron states. However, these potentials remain nearly flat bottom for all configurations of interest.

It is interesting that the addition of ten neutrons to ^{208}Pb triggers larger changes in the radial profile of proton potential than that for neutron one (compare panels (a) and (b) in Fig. 1). The proton potentials of the "Conf- $1i_{11/2}$ " and "Conf- $2g_{9/2}$ " configurations in ^{218}Pb are almost identical in the energy range between -20 MeV and 0.0 MeV [see Fig. 1(a)]. At lower energies, the radius of the proton potential of the "Conf- $1i_{11/2}$ " configuration is smaller than that of the "Conf- $2g_{9/2}$ " one and this difference increases with decreasing energy.

Fig. 2 shows total proton and neutron densities of the configurations under study. Neutron and proton densities of ^{208}Pb serve as the references with respect of which the effect of the occupation of the neutron $1i_{11/2}$ and $2g_{9/2}$ subshells on total neutron and proton densities is

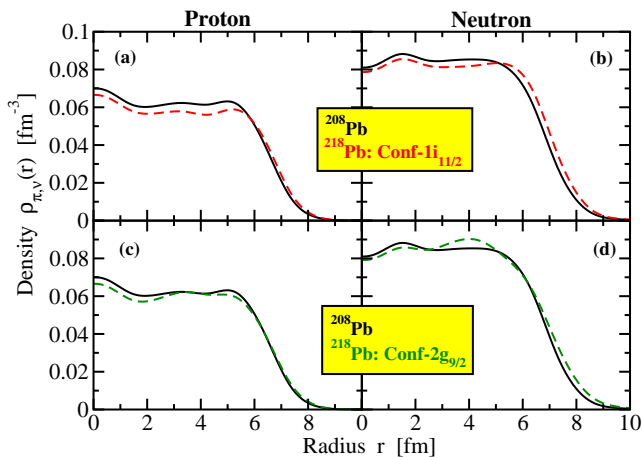


FIG. 2. Proton and neutron densities as a function of radial coordinate r for indicated configurations.

discussed. The occupation of the neutron $1i_{11/2}$ subshell in ^{218}Pb ("Conf- $1i_{11/2}$ ") builds the neutron density mostly in the near-surface and surface regions [see Fig. 2(b)] since the single peak of its single-particle density is located at $r \approx 6.3$ fm (see Fig. 6(z) in Ref. [26]). In contrast, the occupation of the neutron $2g_{9/2}$ subshell in ^{218}Pb ("Conf- $2g_{9/2}$ ") builds the neutron density both in the subsurface and surface regions [see Fig. 2(d)]. This is due to the nodal structure of the wave function of the $2g_{9/2}$ subshell which has two peaks in the single-particle density distribution: the large peak at $r \approx 4.4$ fm and the smaller one at $r \approx 7.8$ fm (see Fig. 6(x) in Ref. [26]).

Because of the isovector force, which tries to keep the neutron and proton density profiles alike, the neutron density changes discussed above feed back into proton densities [see Figs. 2(a) and (c)]. As compared with proton densities in ^{208}Pb , the occupation of either neutron $1i_{11/2}$ or $2g_{9/2}$ subshells leads to the reduction of the proton densities in the central and subsurface regions and increases the density in the surface region. These changes are more pronounced in the case of the occupation of the neutron $1i_{11/2}$ subshell (the "Conf- $1i_{11/2}$ " configuration in ^{218}Pb).

Note that there are intricate and sometimes counter-intuitive interplays between the changes in the densities and nucleonic potentials the origin of which was discussed in detail in Sec. V of Ref. [26]. For example, the density changes on going from the ground state configuration in ^{208}Pb to the configurations in ^{218}Pb show larger increase in the radial profile of neutron densities as compared with proton ones (see Fig. 2). In contrast, the respective changes in the radial profiles of proton potentials of the configurations in ^{218}Pb with respect of that in ^{208}Pb are larger than those for neutron potentials (see Fig. 1).

B. Proton single-particle states

Another consequence of the increase of neutron number on going from ^{208}Pb to ^{218}Pb is the lowering of the energies of the single-particle states in proton potential (see Fig. 3). The energies of spherical subshells located at energies higher than -40 MeV in the "Conf- $1i_{11/2}$ " and "Conf- $2g_{9/2}$ " configurations of ^{218}Pb are lower than those in the ground state configuration of ^{208}Pb . Such lowering implies some reduction of the rms proton radius as compared with the one at the energy of the subshell corresponding to the ground state configuration of ^{208}Pb . However, as follows from further discussion the effect is rather marginal.

Note that there is either small or no energy splitting between the energies of a given proton subshell calculated in these two configurations of ^{218}Pb if the principal quantum number n of the subshell is either $n = 2$ or $n = 3$ (see Fig. 3). In contrast such energy splitting is typically large for the subshells with $n = 1$. These features are not very important for charge radii in the calculations without pairing. However, they are more important in the calculations with pairing since the shifts of the energies of spherical subshells can affect their occupation probabilities in the vicinity of the Fermi level (see discussion in Refs. [3, 22]).

Deeply lying $1s_{1/2}$, $1p_{3/2}$ and $1p_{1/2}$ spherical subshells are affected by the properties and modifications (as compared with ^{208}Pb one) of the bottom of the proton potential which shows the development of wine bottle potential features (see Ref. [26]). These features are most/least pronounced in the "Conf- $2g_{9/2}$ "/"Conf- $1i_{11/2}$ " configurations of ^{218}Pb (see Fig. 3). As a consequence, for a given spherical subshell the calculated energies are almost the same in the ground state configuration of ^{208}Pb and in the "Conf- $1i_{11/2}$ " configurations of ^{218}Pb but significantly lower for the "Conf- $2g_{9/2}$ " configuration of ^{218}Pb . Note that the presence of classically forbidden region in proton potential at small radial coordinate r can significantly modify the density distribution of the $1s_{1/2}$ subshell in the "Conf- $2g_{9/2}$ " configuration of ^{218}Pb and can have some impact on density distribution of this subshell in other two configurations under study (see detailed discussion in Sec. IV of Ref. [26]).

C. Differential charge radii: microscopic origin of the kinks

It is well established in different model calculations that dominant or significant occupation of the neutron $1i_{11/2}$ subshell above the $N = 126$ shell closure is critical for explaining the kink in differential charge radii at neutron $N = 126$ shell closure [3, 8, 16, 18, 20–22]. The functionals (typically CEDFs) in which the $\nu 1i_{11/2}$ subshell is located below the $\nu 2g_{9/2}$ subshell reasonably well describe this kink and the slopes of differential charge

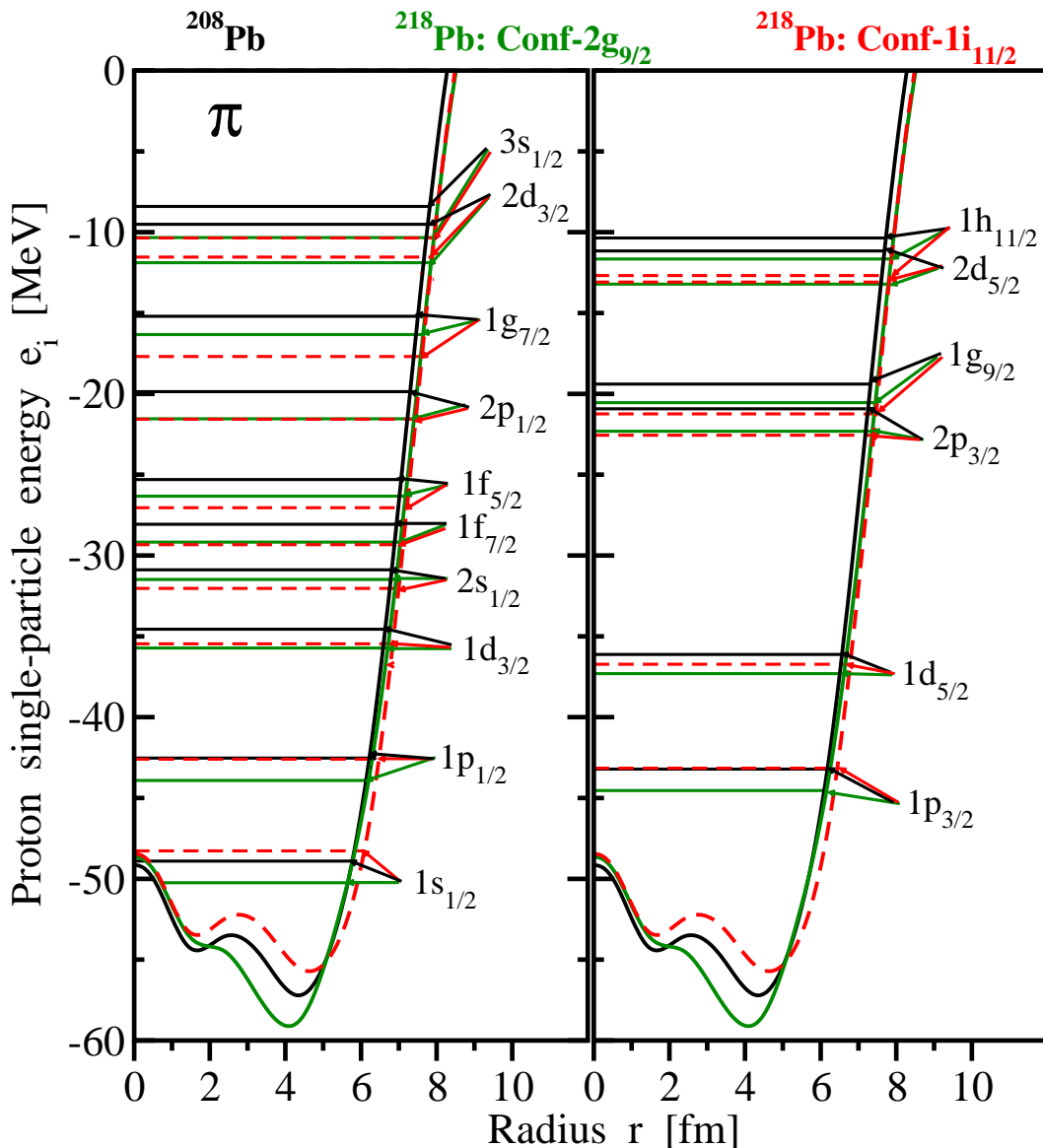


FIG. 3. The energies of proton single-particle states in the proton potentials of indicated nucleonic configurations. Note that only the states below the magic $Z = 82$ shell closure are shown. The figure is split into two panels in order to make it more understandable and to avoid overlapping single-particle states.

radii below and above $N = 126$. In contrast, the functionals (typically non-relativistic ones) with opposite location of two subshells either fail to describe the kink or significantly underestimate its magnitude.

This difference in the slope of differential charge radii above the $N = 126$ shell closure as emerging due to the occupation of above mentioned neutron spherical subshells has been discussed earlier within unpaired RMF calculations with the NL3* CEDF (see discussion of Fig. 4 in Ref. [3]). The differential charge radii $\delta \langle r^2 \rangle_p^{136,126}$ are 1.31 fm^2 and 0.61 fm^2 for the "Conf-1*i*_{11/2}" and "Conf-2*g*_{9/2}" configurations of ^{218}Pb , respectively. However, the microscopic origin of this significant difference has not been investigated. To fill the gap in our knowl-

edge, we show in Tables I and II the contributions of different spherical subshells into build-up of differential charge radii of the "Conf-1*i*_{11/2}" and "Conf-2*g*_{9/2}" configurations of ^{218}Pb . Note that for the sake of comparison with single-particle wave functions and densities we also consider proton single-particle rms radii r_i^p in these tables.

Table I clearly shows that when the neutron 1*i*_{11/2} subshell is occupied in ^{218}Pb the largest changes in proton single-particle rms radii δr_i^p take place for the proton subshells with principal quantum number $n = 1$. The δr_i^p values for the *s*, *p* and *d* $n = 2$ subshells are smaller than the average δr_i^p value over the $n = 1$ subshells by a factor of approximately 2, 5 and 25, respectively. Proton

TABLE I. The contribution of different spherical subshells (column 7) into the build-up of differential charge radii of the "Conf-1*i*_{11/2}" configuration in ²¹⁸Pb. The ground state configuration in ²⁰⁸Pb is used here as a reference. Proton subshells occupied below the *Z* = 82 shell closure are shown in column 1. Their single-particle energies *e_i* [in MeV] are shown in columns 2 and 3 for two configurations under study. Their proton single-particle rms radii *r_i^p* are displayed in columns 4 and 5. The column 6 shows the change of proton single-particle radii $\delta r_i^p = r_i^p(^{218}\text{Pb}[\text{Conf-1}i_{11/2}]) - r_i^p(^{208}\text{Pb})$. Column 7 shows differential single-particle proton radii $\Delta \langle r^2 \rangle_i^{N,N'}$ of the single-particle state belonging to the *i*-th proton subshell. The overlaps of proton and neutron wave functions $\langle \Psi_n^k | \Psi_p^i \rangle$ are shown in column 8. The results for spherical subshells with principal quantum number *n* = 1 are shown in bold. The total quantities given in the last line are calculated using Eq. (8) (column 7) and equations similar to it (columns 4, 5 and 6).

subshell	<i>e_i</i> (²⁰⁸ Pb)	<i>e_i</i> (²¹⁸ Pb)	<i>r_i^p</i> (²⁰⁸ Pb)	<i>r_i^p</i> (²¹⁸ Pb)	δr_i^p	$\Delta \langle r^2 \rangle_i^{N,N'}$	$\langle \Psi_n^k \Psi_p^i \rangle$
1	2	3	4	5	6	7	8
1 <i>s</i> _{1/2}	-48.905	-48.271	4.064254	4.235252	0.170998	1.419199	0.570778
1 <i>p</i> _{3/2}	-43.211	-43.156	4.663197	4.846186	0.182989	1.740112	0.729091
1 <i>p</i> _{1/2}	-42.529	-42.598	4.582763	4.771297	0.188534	1.763556	0.694871
1 <i>d</i> _{5/2}	-36.118	-36.727	5.105879	5.283008	0.177129	1.840178	0.795503
1 <i>d</i> _{3/2}	-34.559	-35.462	4.981504	5.159900	0.178396	1.809189	0.795142
2 <i>s</i> _{1/2}	-30.886	-32.032	4.450498	4.528233	0.077735	0.697962	-0.638347
1 <i>f</i> _{7/2}	-28.068	-29.330	5.479627	5.643146	0.163519	1.818783	0.899794
1 <i>f</i> _{5/2}	-25.298	-27.044	5.334254	5.490660	0.156406	1.693085	0.837178
2 <i>p</i> _{3/2}	-20.924	-22.559	4.985584	5.017296	0.031712	0.317213	-0.571543
2 <i>p</i> _{1/2}	-19.865	-21.566	5.004156	5.031929	0.027773	0.278730	-0.583835
1 <i>g</i> _{9/2}	-19.396	-21.242	5.816346	5.962968	0.146622	1.727100	0.910026
1 <i>g</i> _{7/2}	-15.205	-17.693	5.682103	5.807857	0.125754	1.444908	0.932110
2 <i>d</i> _{5/2}	-11.163	-13.089	5.522224	5.527597	0.005373	0.059372	-0.521033
1 <i>h</i> _{11/2}	-10.360	-12.684	6.129798	6.257349	0.127551	1.579994	0.975584
2 <i>d</i> _{3/2}	-9.513	-11.537	5.580005	5.584444	0.004439	0.049559	-0.554369
3 <i>s</i> _{1/2}	-8.405	-10.360	5.489444	5.476911	-0.012533	-0.137438	0.448467
Total			5.450221	5.569299	0.119078	1.312261	

TABLE II. The same as in Table I but for the "Conf-2*g*_{9/2}" configuration in ²¹⁸Pb. The results for spherical subshells with principal quantum number *n* = 2 are shown in bold.

subshell	<i>e_i</i> (²⁰⁸ Pb)	<i>e_i</i> (²¹⁸ Pb)	<i>r_i^p</i> (²⁰⁸ Pb)	<i>r_i^p</i> (²¹⁸ Pb)	δr_i^p	$\Delta \langle r^2 \rangle_i^{N,N'}$	$\langle \Psi_n^k \Psi_p^i \rangle$
1	2	3	4	5	6	7	8
1 <i>s</i> _{1/2}	-48.905	-50.239	4.064254	4.062288	-0.001966	-0.015978	0.399380
1 <i>p</i> _{3/2}	-43.211	-44.539	4.663197	4.631773	-0.031424	-0.292086	0.345824
1 <i>p</i> _{1/2}	-42.529	-43.915	4.582763	4.535377	-0.047386	-0.432074	0.373550
1 <i>d</i> _{5/2}	-36.118	-37.305	5.105879	5.092180	-0.013699	-0.139704	0.273309
1 <i>d</i> _{3/2}	-34.559	-35.720	4.981504	4.962466	-0.019038	-0.189316	0.282916
2 <i>s</i> _{1/2}	-30.886	-31.484	4.450498	4.565793	0.115295	1.039534	0.182596
1 <i>f</i> _{7/2}	-28.068	-29.174	5.479627	5.496088	0.016461	0.180670	0.119881
1 <i>f</i> _{5/2}	-25.298	-26.329	5.334254	5.363151	0.028897	0.309126	0.186386
2 <i>p</i> _{3/2}	-20.924	-22.315	4.985584	5.158503	0.172919	1.754108	0.475303
2 <i>p</i> _{1/2}	-19.865	-21.544	5.004156	5.170061	0.165905	1.687954	0.447216
1 <i>g</i> _{9/2}	-19.396	-20.544	5.816346	5.862341	0.045995	0.537159	-0.000955
1 <i>g</i> _{7/2}	-15.205	-16.330	5.682103	5.757601	0.075498	0.863670	-0.000587
2 <i>d</i> _{5/2}	-11.163	-13.214	5.522224	5.663334	0.14111	1.578392	0.754258
1 <i>h</i> _{11/2}	-10.360	-11.659	6.129798	6.199679	0.069881	0.861599	-0.182783
2 <i>d</i> _{3/2}	-9.513	-11.887	5.580005	5.686162	0.106157	1.195982	0.719801
3 <i>s</i> _{1/2}	-8.405	-10.335	5.489444	5.540033	0.050589	0.557970	-0.7388235
Total			5.450221	5.505978	0.055757	0.6110	

single-particle rms radius of the 3*s*_{1/2} subshell even decreases on transition from the ground state configuration of ²⁰⁸Pb to the "Conf-1*i*_{11/2}" configuration of ²¹⁸Pb. All these changes are reflected in differential single-particle proton radii $\Delta \langle r^2 \rangle_i^{N,N'}$ (see column 7 of Table I) so that 96.7% of differential charge radius $\delta \langle r^2 \rangle_p^{136,126} = 1.31$

fm² [see Eq. (3)] of the "Conf-1*i*_{11/2}" configuration in ²¹⁸Pb with respect of the ground state configuration in ²⁰⁸Pb are built by the *n* = 1 proton subshells.

The situation drastically changes when the neutron 2*g*_{9/2} subshell is occupied in ²¹⁸Pb [configuration "Conf-2*g*_{9/2}"] (see Table II). In this case, the largest δr_i^p values

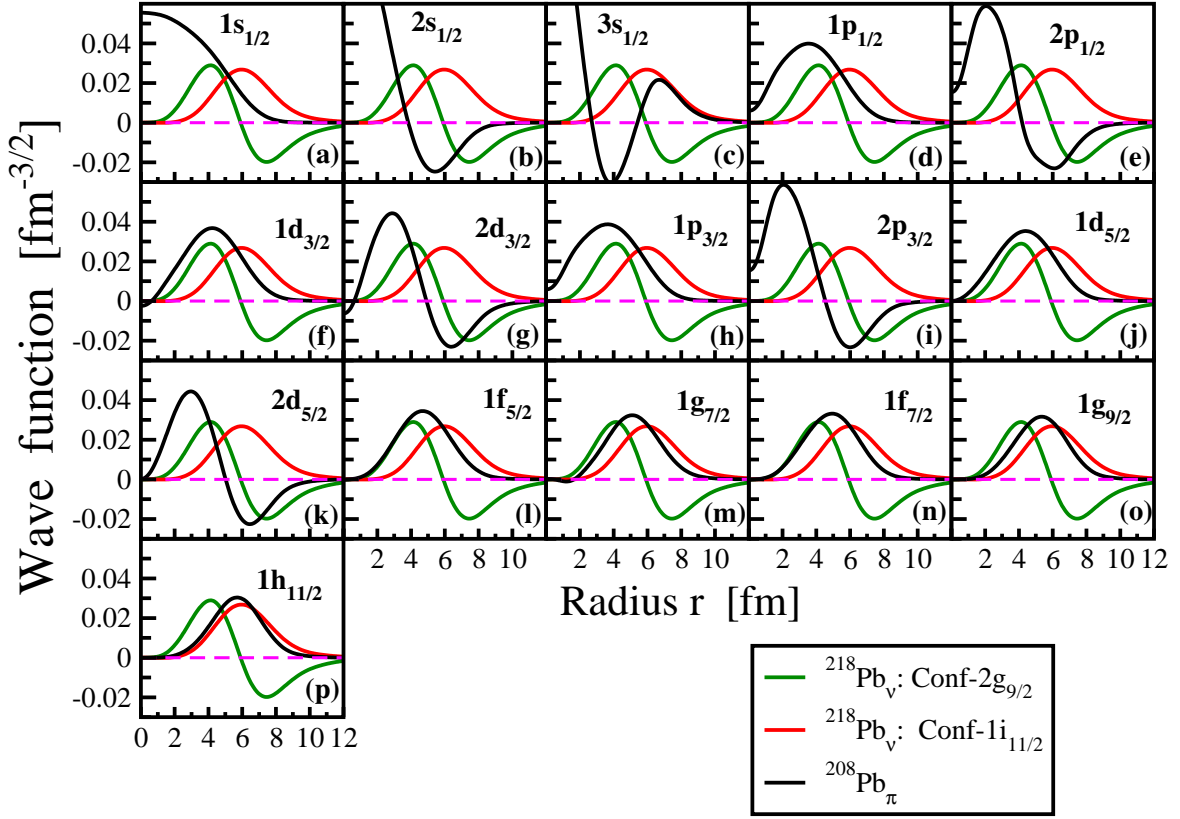


FIG. 4. Single-particle wave functions of proton (black curves) spherical subshells in ^{208}Pb nucleus compared with those of the neutron $2g_{9/2}$ (green lines) and $1i_{11/2}$ (red lines) subshells. Note that the latter two states are shown in each panel. Proton subshell labels are shown on each panel.

are seen for the $2s_{1/2}$, $2p_{3/2}$, $2p_{1/2}$, $2d_{5/2}$ and $2d_{3/2}$ proton subshells. The proton rms radii of low lying $1s_{1/2}$, $1p_{3/2}$, $1p_{1/2}$, $1d_{5/2}$ and $1d_{3/2}$ subshells even decrease on transition from the ground state configuration of ^{208}Pb to the "Conf- $2g_{9/2}$ " configuration of ^{218}Pb . This is the consequence of self-consistency effects discussed in Secs. III A and III B and the effects discussed in Sec. III D. In addition, the increase of proton rms radii is rather modest for remaining $n = 1$ subshells and for the $3s_{1/2}$ subshell. All these changes are reflected in differential single-particle proton radii $\Delta \langle r^2 \rangle_i^{N,N'}$ (see column 7 of Table II) so that 53.3% of differential charge radius $\delta \langle r^2 \rangle_p^{136,126} = 0.61 \text{ fm}^2$ of two configurations under study are built by the $n = 2$ proton subshells. This is despite the low multiplicity of the occupied $n = 2$ subshells which represent only approximately 22% of the occupied single-particle states of the $Z = 82$ core.

The impact of the occupation of neutron $2g_{9/2}$ subshell on proton single-particle rms radii of the $n = 2$ proton subshells (see Table II) is on average comparable to the one of neutron $1i_{11/2}$ subshell on proton single-particle rms radii of the $n = 1$ proton subshells (see Table I). Thus, other factors have to be involved to explain large difference in differential charge radii of the "Conf- $1i_{11/2}$ " and "Conf- $2g_{9/2}$ " configurations in ^{218}Pb . In-

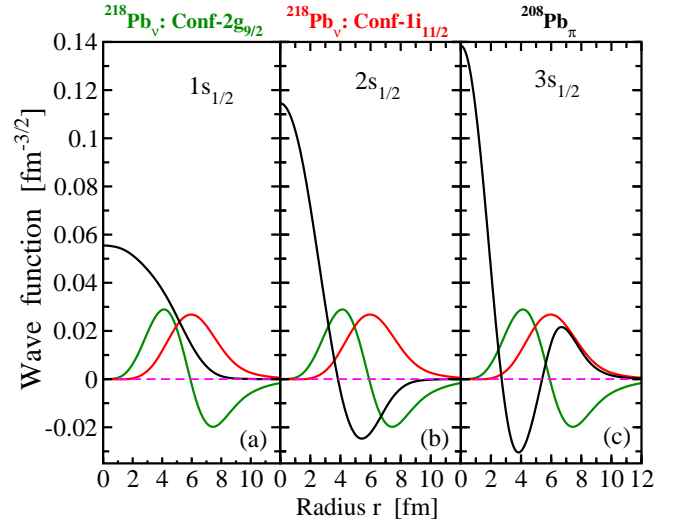


FIG. 5. The same as Fig. 4 but only for the proton s states and with enlarged range on vertical axis.

deed, the analysis of Eq. (8) clearly indicates that differential charge radii between two isotopes are defined not only by the differential single-particle radii $\Delta \langle r^2 \rangle_i^{N,N'}$ of occupied single-particle states

but also by the abundance of the subshells with a given n among occupied subshells and their multiplicity m_i . Low n subshells are most abundant in any nucleonic potential (see Refs. [26, 32]). Indeed, there are 10 $n = 1$, 5 $n = 2$ and 1 $n = 3$ occupied subshells in the $Z = 82$ core of the Pb isotopes (see Fig. 3). In addition the $n = 1$ subshells have the highest multiplicity m_{max} among the occupied subshells: $m_{max} = 12, 6$ and 2 for the $n = 1, 2$ and 3 subshells, respectively. As a result, 62, 18 and 2 protons of the $Z = 82$ core are located in the $n = 1, 2$ and 3 subshells, respectively. The combination of all above mentioned in this subsection factors allows to explain large difference in differential charge radii of the "Conf- $1i_{11/2}$ " and "Conf- $2g_{9/2}$ " configurations in ^{218}Pb .

D. Microscopic origin of the pull of neutron subshells on proton ones

In order to better understand the state dependence of the pull provided by a neutron in a given state on the proton in the nlj subshell, Figs. 4 and 5 compare the proton wave functions of all occupied proton subshells in the $Z = 82$ core of the ^{208}Pb nucleus with the neutron wave functions of the neutron $1i_{11/2}$ and $2g_{9/2}$ subshells calculated in the "Conf- $1i_{11/2}$ " and "Conf- $2g_{9/2}$ " configurations of ^{218}Pb , respectively. In addition, the overlap of respective proton and neutron wave functions defined as

$$\langle \Psi_n^k | \Psi_p^i \rangle = \int \Psi_n^k(\vec{r}) \Psi_p^i(\vec{r}) d^3r \quad (16)$$

is presented in the last columns of Tables I and II. Here proton state index i runs over all occupied proton subshells while neutron index k is equal either to $k = 1i_{11/2}$ or $k = 2g_{9/2}$. Positive (negative) values of these overlaps indicate that the wave functions Ψ_n^k and Ψ_p^i are spatially mostly in phase (out of phase).

Let us first consider the overlaps of proton wave functions with the neutron $\nu 1i_{11/2}$ one [see Table I]. The largest overlap exists for the $\pi 1h_{11/2}$ state ($\langle \Psi_n^k | \Psi_p^i \rangle = 0.98$). Indeed, these two states have the wave functions which are most similar among considered cases [see Fig. 4(p) and compare it with other panels of this figure]. The degree of the similarity ($\langle \Psi_n^k | \Psi_p^i \rangle \approx 0.92$) of the wave function of the neutron $\nu 1i_{11/2}$ subshell is somewhat smaller with the wave functions of the proton $\pi 1g_{7/2}$ and $\pi 1g_{9/2}$ subshells [see Fig. 4(m) and (o)]. With decreasing the single-particle energy of spherical $n = 1$ proton subshell the degree of the similarity between neutron and proton wave functions given by $\langle \Psi_n^k | \Psi_p^i \rangle$ decreases but still remains high (see the last column of Table I and Figs. 4(l), (j), (h), (f), (d) and (a)). Among the proton $n = 1$ subshells the lowest overlap $\langle \Psi_n^k | \Psi_p^i \rangle = 0.57$ exists for proton $1s_{1/2}$ subshell which is the only $n = 1$ subshell with the maximum of the wave function at the center of nucleus [see Fig. 4(a)].

The situation is completely different for the proton subshells with $n = 2$: the evolution of their wave functions as a function of radial coordinate r is mostly out of phase with that of the wave function of the proton $1i_{11/2}$ subshell [see Figs. 4(b), (e), (g), (i) and (k)]. This is due to the differences in the nodal structure of these wave functions. As a consequence, large negative overlaps $\langle \Psi_n^k | \Psi_p^i \rangle$ exist for these pairs of the states (see last column of Table I). There are large differences due to underlying nodal structure between the wave functions of the proton $3s_{1/2}$ and neutron $1i_{11/2}$ subshells (see Fig.

4
t]
is
k

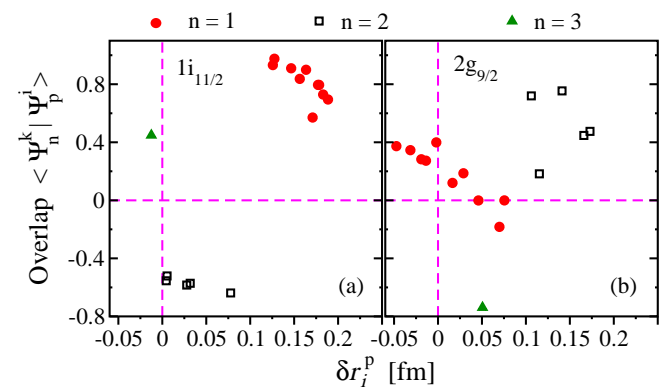


FIG. 6. The correlations between the overlaps $\langle \Psi_n^k | \Psi_p^i \rangle$ and the changes of proton single-particle radii δr_i^p for proton subshells of the $Z = 82$ core. Solid red circles, open black squares and green triangles are used for the $n = 1, n = 2$ and $n = 3$

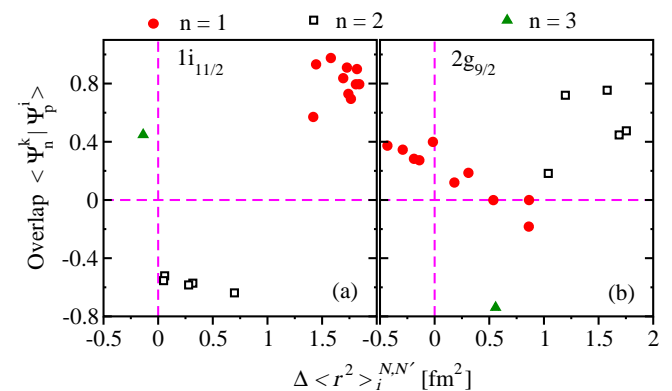


FIG. 7. The same as in Fig. 6 but for the correlations between the overlaps $\langle \Psi_n^k | \Psi_p^i \rangle$ and differential single-particle proton radii $\Delta \langle r^2 \rangle_i^{N,N'}$.

The occupation of the neutron $2g_{9/2}$ subshell leads to completely different pattern of behavior (see Figs. 4

and 5 and Table II). The largest overlaps exist for the $n = 2$ proton subshells: the only exception is the overlap which includes proton $2s_{1/2}$ subshell which has a maximum of its wave function at $r = 0$. These overlaps become smaller or even negative for the cases which include $n = 1$ and $n = 3$ proton subshells (see the last column in Table II).

Fig. 6 shows the correlations between the overlaps $\langle \Psi_n^k | \Psi_p^i \rangle$ for the neutrons in the $1i_{11/2}$ and $2g_{9/2}$ subshells and the proton subshells occupied in the $Z = 82$ core and the changes in single-particle proton rms radii δr_i^p of these subshells triggered by the occupation of respective neutron subshells. In general, the largest δr_i^p values appear for the proton subshells which have the same principal quantum number n as occupied neutron subshell. This also corresponds to the largest positive overlaps $\langle \Psi_n^k | \Psi_p^i \rangle$. Small or negative overlaps, which correspond to the case of different principal quantum numbers n of proton and neutron subshells, typically lead to relatively small δr_i^p values.

These correlations are very pronounced in the case of the occupation of the neutron $1i_{11/2}$ subshell since its wave function has a simple structure with a single maximum at $r \approx 6$ fm (see Fig. 4). Significant changes in the single-particle rms radius are seen for proton $n = 1$ subshells which have large overlaps $\langle \Psi_n^k | \Psi_p^i \rangle$ but rather small δr_i^p values exist for the proton $n = 2$ subshells which have negative overlaps (see Fig. 6 and Table I).

Such correlations are somewhat less pronounced in the case of the occupation of the $2g_{9/2}$ neutron subshell the wave function of which has maximum at $r \approx 4$ fm and minimum at $r = 7.5$ fm (see Fig. 4). The largest overlaps $\langle \Psi_n^k | \Psi_p^i \rangle$ are seen with proton $n = 2$ $2p_{3/2}$, $2p_{1/2}$, $2d_{5/2}$ and $2d_{3/2}$ subshells which produce the largest changes in the proton single-particle rms radii (see Fig. 6 and Table II). Smaller and sometimes negative changes in the proton single-particle rms radii are produced for the $n = 1$ and $n = 3$ proton subshells when neutron $2g_{9/2}$ subshell becomes occupied.

Note that similar to above discussed correlations are also seen between $\langle \Psi_n^k | \Psi_p^i \rangle$ and differential single-particle proton radii $\Delta \langle r^2 \rangle_i^{N,N'}$ (see Fig. 7) with the latter quantities defining the differential charge radius between two isotopes [see Eq. (8)].

The absolute values of the $\langle \Psi_n^k | \Psi_p^i \rangle$ overlaps presented in column 8 of Tables I and II are similar to those obtained in Skyrme DFT calculations with NRAPRii energy density functional (see Fig. 5 of Ref. [21]). This clearly indicates a similar mechanism of the buildup of differential charge radii in non-relativistic and covariant DFTs.

Because of the dependence of charge radii and their changes on proton single-particle densities (see Sec. II), a deeper microscopic insight is provided by the analysis of the redistributions of the proton single-particle densities defined as

$$\delta \rho_i^p(r) = \rho_i^p(r)[^{218}\text{Pb} - \text{conf}] - \rho_i^p(r)[^{208}\text{Pb}] \quad (17)$$

when different neutron subshells are occupied in ^{218}Pb . Since the single-particle density is normalized to unity [see Eq. (5)], the addition of neutron(s) to the ^{208}Pb nucleus will only lead to redistribution of the proton single-particle density under the condition that

$$\int r^2 \delta \rho_i^p(r) = 0 \quad (18)$$

These redistributions are clearly seen in Fig. 8. Let us consider as an example the changes in the single-particle proton densities of the $1p_{3/2}$ subshell [see Fig. 8(h)]. The occupation of the neutrons in the $2g_{9/2}$ subshell (the "Conf- $2g_{9/2}$ " configuration in ^{218}Pb) leads to an increase of proton densities of the $1p_{3/2}$ subshell at $r \approx 3.2$ fm and their decrease at $r \approx 5.5$ fm as compared with that in the ground state configuration of ^{208}Pb [green line in Fig. 8(h)]. In contrast, the occupation of the neutrons in the $1i_{11/2}$ subshell (the "Conf- $1i_{11/2}$ " configuration in ^{218}Pb) has an opposite effect: it leads to the decrease of proton densities of the $1p_{3/2}$ subshell at $r \approx 3$ fm and their increase⁴ at $r \approx 6$ fm [red line in Fig. 8(h)]. Note that the number of the oscillations of density redistributions increases with the increase of principal quantum number n of the proton and neutron subshells involved (compare, for example, the panels (c) and (h) of Fig. 8).

For almost all proton subshells of the $Z = 82$ core the occupation of the $1i_{11/2}$ or $2g_{9/2}$ neutron subshells leads to drastically different redistributions of proton single-particle densities which are frequently out of phase of each others as a function of radial coordinate r (see Fig. 8). Thus, for a given proton subshell this leads to different changes in the proton single-particle radii δr_i^p and substantial differences in differential single-particle radii $\Delta \langle r^2 \rangle_i^{N,N'}$ (compare Tables I and II).

IV. GENERAL OBSERVATIONS

A. The origin of differential charge radii

The detailed analysis presented in Sec. III clearly indicates that the change of differential charge radius with increasing neutron number has a single-particle origin. Added neutron interacts with proton in a given subshell and this leads to a redistribution of single-particle densities of occupied proton states which in turn modifies the charge radii. The outcome of this interaction depends on the relative properties of the wave functions

⁴ The reader should not be confused by larger density changes at low radial coordinates as compared with those at larger values of r . This is because the density plots as a function of radial coordinate tend to overemphasize the importance of the central region since they ignore the fact that the number of particles dn in a spherical shell of thickness dr is given by $4\pi r^2 \rho(r) dr$ (see example in Sec. III of Ref. [26]).

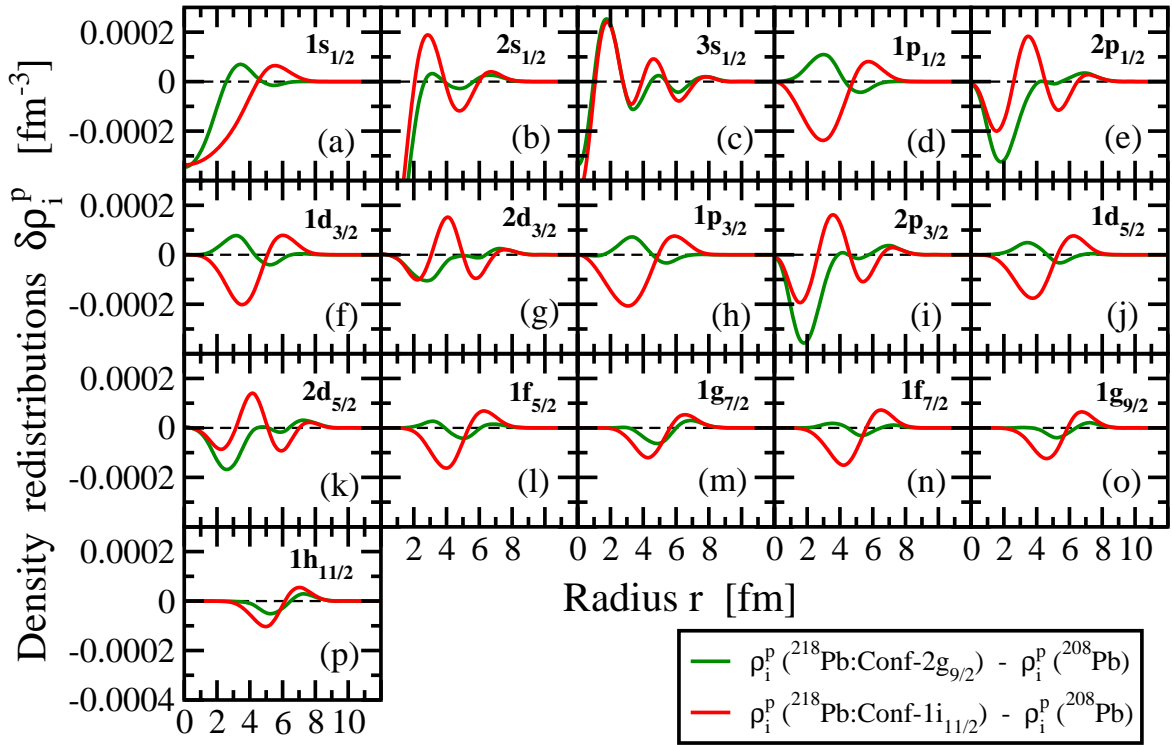


FIG. 8. Proton single-particle density redistributions $\delta\rho_i^p(r)$ caused by the occupation of indicated neutron subshells in ^{218}Pb (see text for details).

of interacting proton and neutron. Large positive overlap $\langle \Psi_n^k | \Psi_p^k \rangle$ between their wave functions leads to a substantial increase of differential single-particle charge radius of proton subshell in which interacting proton is located. In contrast, small or negative overlap of their wave functions typically leads to either small increase or even decrease in differential single-particle charge radius.

Ref. [21] has discussed the pull on the proton states provided by the occupation of neutron states and resulting change in charge radii as emerging from strong nuclear symmetry energy. However, our detailed analysis clearly indicates that the changes in charge radii with increasing neutron number are governed by the proton-neutron interaction.

The buildup of differential charge radii $\delta\langle r^2 \rangle_p^{N,N'}$ between two isotopes is also a collective phenomenon since all occupied proton states contribute to it [see Eq. (8)] and none of these states provides a dominant contribution to $\delta\langle r^2 \rangle_p^{N,N'}$ (see Tables I and II).

B. Applicability of alternative models to the description of differential charge radii in deformed nuclei

As reviewed in the introduction of Ref. [3], the absolute majority of the studies of differential charge radii has been performed either in DFT or in ab initio approaches.

However, it is well known that DFT models have some deficiencies in the description of spectroscopic properties related to the energies of the single-particle states and their wave functions [33–37]. Moreover, the performance of ab initio models in the description of single-particle spectra in odd- A nuclei is comparable with that for the DFT models but such calculations are available only for light nuclei (see Refs. [38–41]). In contrast, spherical shell models with empirical interactions provide a better description of experimental spectroscopic data in spherical nuclei located in the vicinity of doubly magic nuclei and microscopic+macroscopic (mic+mac) models based on phenomenological potentials such as the Woods-Saxon one does the same in the region of deformed nuclei. However, these models are not expected to be adequate for the description of differential charge radii due to the reasons mentioned below.

The lack of self-consistency effects and the interaction between protons and neutrons will affect the description of differential charge radii in the mic+mac model. This is because the addition of neutron does not affect the proton subsystem in a self-consistent manner on the level of single-particle subshells via the mechanisms discussed in Sec. III. For example, in the Woods-Saxon potential it affects the total radius R of nucleus only via mass dependence $R = 1.2A^{1/3}$. This means that the occupation of the neutron $1i_{11/2}$ and $2g_{9/2}$ subshells in the $N > 126$ Pb isotopes will lead to the same differential charge radii contrary to the results of self-consistent cal-

culations (see Refs. [3, 8, 18]). Moreover, there is a lack of self-consistency in the definition of the radial properties of the density distributions in the macroscopic (liquid drop) and microscopic (single-particle potential) parts of the mic+mac model. To our knowledge, this aspect of the problem has not been studied in detail. However, the physical observables similar to $\delta \langle r^2 \rangle_p^{N,N'}$, namely, relative charge quadrupole moments of superdeformed bands are affected by the lack of self-consistency between microscopic and macroscopic parts (see Ref. [42]).

Although the spherical shell model takes into account the proton-neutron interaction it suffers from the introduction of the core. As a consequence, the pull provided by extra neutron(s) on the proton single-particle states forming the core is ignored and this affects drastically the calculated charge radii of the nuclei with valence nucleons outside the core. This introduces uncontrollable errors in the calculations of differential charge radii and thus severely limits the applicability of spherical shell model to the description of this observable. Few existing calculations of differential charge radii in spherical shell model (see Refs. [43, 44]) suffer from this problem. For example, they cannot reproduce the kink in the differential charge radii of the Sn isotopes at $N = 82$ and Pb isotopes at $N = 126$ [44]. This problem can be rectified by employing no-core shell model but because of numerical reasons such models are applicable only to light nuclei [45, 46].

C. Potential mechanisms affecting odd-even staggering (OES) in charge radii

Several mechanisms of regular and inverted OES in charge radii have been discussed and reviewed in Sec. IX of Ref. [3]. These include shape coexistence leading to deformation staggering in even and odd- A nuclei (see Sec. IXA of Ref. [3]), pairing correlations (see Sec. IXB of Ref. [3]), particle-vibration coupling (PVC) in odd- A nuclei (see Sec. IXC of Ref. [3]) and some other mechanisms (see Sec. IXD of Ref. [3]). The PVC mechanism is responsible for a substantial fragmentation of the wave function of the ground states in spherical odd- A nuclei (see Sec. IXC of Ref. [3]) and rearrangement of the energies of the predominantly single-particle states (see Ref. [20]).

Here we extend the discussion presented in Sec. IX of Ref. [3] and outline other potential mechanisms which could affect OES in charge radii. This discussion is based on the fact that it is the single-particle content of unpaired neutron states in odd- N nuclei which defines the pull on proton densities (see present paper and Refs. [3, 21]). If the deformation changes between neighbouring even-even and odd- A nuclei are small, this is dominant mechanism defining OES in charge radii.

If the structure of extra neutron states does not change with their sequential addition, the differential charge radii show a linear evolution as a function of neutron

number (see discussion of Fig. 4 in Ref. [3]) and no OES in charge radii is present. However, if the structure of the neutron state in odd- N nuclei is affected by the interaction(s) or effect(s) not present in its even-even neighbors (such as blocking effect for pairing [11–13]) and/or particle-vibration coupling [3, 20]), this leads to OES in charge radii.

The transition to deformed nuclei opens additional channels which are not present in spherical ones but which can affect OES in charge radii. These are the Coriolis interaction in odd and odd-odd nuclei and residual interaction of unpaired proton and neutron in odd-odd nuclei: each of them affects the structure of the wave function in odd- N nuclei as compared with the ones of their even $N \pm 1$ neighbors and this can contribute to OES in charge radii. To our knowledge these channels have not been indicated in literature as possible sources of OES in charge radii because they are neglected in the DFT calculations.

The admixtures of the vibrational phonons to the structure of the ground states in deformed rare-earth and actinide odd-mass nuclei is relatively small (see Ref. [47–49]) especially when compared with spherical nuclei (see Refs. [37, 50, 51]). Thus, their role in building OES of charge radii is expected to be reduced as compared with the one in spherical nuclei (see Refs. [3, 20]). On the other hand, the Coriolis interaction can be active in the ground states of deformed odd- N nuclei but it is absent in the ground states of even-even nuclei (see Refs. [32, 52]). This interaction leads to a $\Delta K = 1$ mixing⁵ of different states both in odd (see Refs. [52]) and odd-odd (see Refs. [53, 54]) nuclei. If the wavefunction of the ground state of the nucleus with odd- N is strongly affected by Coriolis mixing, this can affect OES of charge radii.

The situation in odd- Z isotopic chains (see Fig. 27 in Ref. [3]) which includes odd-odd nuclei becomes even more complicated for theoretical interpretation since in addition to Coriolis interaction there is the possibility for the $\Delta K = 0$ mixing due to residual interaction of unpaired proton and neutron in odd-odd nuclei [53, 54]. Note that such mixing is typically calculated in the rotor+particle models (PRM) and it is neglected in the state-of-the-art DFT applications. In some cases the $\Delta K = 0$ mixing can be strong so it can potentially have significant impact on the structure of the wave function of odd neutron which generates the pull on proton densities.

Let us consider the isotopic chain of the Eu isotopes which is one of the best examples of inverted OES in charge radii (see Fig. 27 in Ref. [3]). As discussed in Sec. IX of Ref. [3] the inversion of OES at $N \approx 88$ is most likely triggered by the transition from spherical or quasi-spherical nuclei to deformed ones with increasing neutron number. However, such inversion of OES exists also for

⁵ Here K is the projection of single-particle angular momentum on the axis of symmetry of deformed nucleus.

$N = 90, 91$ and 92 which covers deformed nuclei (see Fig. 27(f) in Ref. [3]). The experimental observations (Ref. [55]) and PRM calculations (Ref. [56]) indicate strong $\Delta K = 0$ mixing for the $K^\pi = 1^\pm, 3^\pm$ and 4^\pm bandheads in the ^{154}Eu nucleus including $K^\pi = 3^-$ ground state with the $\pi 5/2[413] - \nu 11/2[505]$ structure. Such mixing is observed and calculated in two-quasiparticle configurations of ^{156}Eu [57] but ground state of this nucleus seems not to be affected by it. These features may lead to the inversion of OES around $N = 91$ and its absence above $N = 92$. In reality, at the neutron numbers of interest the neighboring $Z = 62$ Sm isotopes show regular OES in charge radii (see Fig. 26(1) in Ref. [3]) which suggests that the inversion of OES in charge radii of the Eu ($Z = 63$) isotopes are most likely due to the properties of odd-odd nuclei. The detailed DFT calculations with residual interaction of unpaired proton and neutron in odd-odd nuclei are needed to confirm or reject such an interpretation. However, such investigation goes beyond the scope of the present study.

V. CONCLUSIONS

The self-consistency and proton-neutron interaction effects in the buildup of differential charge radii have been considered by comparing two configurations of the ^{218}Pb nucleus, generated by the occupation of the neutron $1i_{11/2}$ and $2g_{9/2}$ subshells, with the ground state configuration in ^{208}Pb . The main contribution to differential charge radii has a single-particle origin and comes from the interaction of added neutron(s) and the protons forming the $Z = 82$ proton core. This interaction depends on the overlaps of the proton and neutron wave functions and leads to a redistribution of single-particle density of occupied proton states which in turn modifies the charge radii. In contrast, self-consistency effects affecting the shape of proton potential, proton densities and the energies of the single-particle states in the proton potential provide only a small contribution. Note that

the buildup of differential charge radii between two isotopes is also a collective phenomenon since all occupied proton single-particle states contribute to it. Although these results were obtained for the Pb isotopes, they are general and applicable to any isotopic chain.

This combination of single-particle and collective aspects in the building of differential charge radii limits the applicability of different classes of the models to the description of this physical observable. The models which ignore self-consistency effects and proton-neutron interaction (such as microscopic+macroscopic model) cannot describe this physical observable. The models which ignore collective aspect of the problem by introducing the core (such as spherical shell model) introduce uncontrollable errors in the description of differential charge radii.

The pull provided by an extra neutron on proton states depends on the structure of the state occupied by it. For deformed even- Z nuclei, the wave function of the ground states in odd- N nuclei is more complicated than that of the ground states in neighboring even-even nuclei because of the presence of the Coriolis interaction. The addition of proton (odd- Z nuclei) leads to a further complication of the wave function since Coriolis interaction is present in all nuclei of isotopic chain under study and, in addition, the structure of odd-odd nuclei is affected by the residual interaction between unpaired proton and neutron. The analysis indicates that both the Coriolis interaction in odd and odd-odd nuclei and the residual interaction between unpaired proton and neutron in odd-odd nuclei could affect the odd-even staggering in charge radii if their impact on the wave function of the ground state of these nuclei is appreciable. Note that these interactions are usually neglected in the DFT calculations.

VI. ACKNOWLEDGMENTS

This material is based upon work supported by the U.S. Department of Energy, Office of Science, Office of Nuclear Physics under Award No. DE-SC0013037.

-
- [1] I. Angeli and K. P. Marinova, *At. Data Nucl. Data Tables* **99**, 69 (2013).
 - [2] P. Campbell, I. Moore, and M. Pearson, *Prog. Part. Nucl. Phys.* **86**, 127 (2016).
 - [3] U. C. Perera, A. V. Afanasjev, and P. Ring, *Phys. Rev. C* **104**, 064313 (2021).
 - [4] S. E. Agbemava, A. V. Afanasjev, D. Ray, and P. Ring, *Phys. Rev. C* **89**, 054320 (2014).
 - [5] R. F. Garcia-Ruiz, M. L. Bissell, K. Blaum, A. Schwenk, J. Simonis, K. A. Wendt, and D. T. Yordanov, *Nature Physics* **12**, 594 (2016).
 - [6] A. Koszorús, X. F. Yang, W. G. Jiang, S. J. Novario, S. W. Bai, J. Billowes, C. L. Binnersley, M. L. Bissell, T. E. Cocolios, B. S. Cooper, R. P. de Groote, A. Ekström, K. T. Flanagan, C. Forssén, S. Franchoo, R. F. Garcia-Ruiz, F. P. Gustafsson, G. Hagen, G. R. Jansen, A. Kanellakopoulos, M. Kortelainen, W. Nazarewicz, G. Neyens, T. Papenbrock, P.-G. Reinhard, C. M. Rickerts, B. K. Sahoo, A. R. Vernon, and S. G. Wilkins, *Nature Physics* **17**, 539 (2021).
 - [7] N. Tajima, P. Bonche, H. Flocard, P.-H. Heenen, and M. S. Weiss, *Nucl. Phys. A* **551**, 434 (1993).
 - [8] P.-G. Reinhard and H. Flocard, *Nucl. Phys. A* **584**, 467 (1995).
 - [9] C. Gorges, L. V. Rodríguez, D. L. Balabanski, M. L. Bissell, K. Blaum, B. Cheal, R. F. Garcia Ruiz, G. Georgiev, W. Gins, H. Heylen, A. Kanellakopoulos, S. Kaufmann, M. Kowalska, V. Lagaki, S. Lechner, B. Maaß, S. Malbrunot-Ettenauer, W. Nazarewicz, R. Neugart, G. Neyens, W. Nörtershäuser, P.-G. Rein-

- hard, S. Sailer, R. Sánchez, S. Schmidt, L. Wehner, C. Wraith, L. Xie, Z. Y. Xu, X. F. Yang, and D. T. Yordanov, *Phys. Rev. Lett.* **122**, 192502 (2019).
- [10] T. Naito, T. Oishi, H. Sagawa, and Z. Wang, nuclear theory archive arXiv:2209.02857v2 [nucl-th] (2022).
- [11] S. A. Fayans, S. V. Tolokonnikov, E. L. Trykov, and D. Zawischa, *Phys. Lett. B* **338**, 1994 (1).
- [12] S. A. Fayans, S. V. Tolokonnikov, E. L. Trykov, and D. Zawischa, *Nucl. Phys. A* **676**, 49 (2000).
- [13] P.-G. Reinhard and W. Nazarewicz, *Phys. Rev. C* **95**, 064328 (2017).
- [14] R. Rodríguez-Guzmán, P. Sarriguren, L. M. Robledo, and S. Perez-Martin, *Phys. Lett. B* **691**, 202 (2010).
- [15] H. Nakada, *Phys. Rev. C* **92**, 044307 (2015).
- [16] H. Nakada and T. Inakura, *Phys. Rev. C* **91**, 021302(R) (2015).
- [17] H. Nakada, *Phys. Rev. C* **100**, 044310 (2019).
- [18] M. M. Sharma, G. A. Lalazissis, and P. Ring, *Phys. Lett. B* **317**, 9 (1993).
- [19] M. M. Sharma, G. Lalazissis, J. König, and P. Ring, *Phys. Rev. Lett.* **74**, 3744 (1995).
- [20] T. D. Goodacre, A. V. Afanasjev, A. E. Barzakh, B. A. Marsh, S. Sels, P. Ring, H. Nakada, A. N. Andreyev, P. V. Duppen, N. A. Althubiti, B. Andel, D. Atanasov, J. Billowes, K. Blaum, T. E. Cocolios, J. G. Cubiss, G. J. Farooq-Smith, D. V. Fedorov, V. N. Fedosseev, K. T. Flanagan, L. P. Gaffney, L. Ghys, M. Huyse, S. Kreim, D. Lunney, K. M. Lynch, V. Manea, Y. M. Palenzuela, P. L. Molkanov, M. Rosenbusch, R. E. Rossel, S. Rothe, L. Schweikhard, M. D. Seliverstov, P. Spagnoletti, C. V. Beveren, M. Veinhard, E. Verstraelen, A. Welker, K. Wendt, F. Wienholtz, R. N. Wolf, A. Zadvornaya, and K. Zuber, *Phys. Rev. Lett.* **126**, 032502 (2021).
- [21] P. M. Goddard, P. D. Stevenson, and A. Rios, *Phys. Rev. Lett.* **110**, 032503 (2013).
- [22] T. Day Goodacre, A. V. Afanasjev, A. E. Barzakh, L. Nies, B. A. Marsh, S. Sels, U. C. Perera, P. Ring, F. Wienholtz, A. N. Andreyev, P. Van Duppen, N. A. Althubiti, B. Andel, D. Atanasov, R. S. Augusto, J. Billowes, K. Blaum, T. E. Cocolios, J. G. Cubiss, G. J. Farooq-Smith, D. V. Fedorov, V. N. Fedosseev, K. T. Flanagan, L. P. Gaffney, L. Ghys, A. Gottberg, M. Huyse, S. Kreim, P. Kunz, D. Lunney, K. M. Lynch, V. Manea, Y. M. Palenzuela, T. M. Medonca, P. L. Molkanov, M. Mougeot, J. P. Ramos, M. Rosenbusch, R. E. Rossel, S. Rothe, L. Schweikhard, M. D. Seliverstov, P. Spagnoletti, C. Van Beveren, M. Veinhard, E. Verstraelen, A. Welker, K. Wendt, R. N. Wolf, A. Zadvornaya, and K. Zuber, *Phys. Rev. C* **104**, 054322 (2021).
- [23] D. Vretenar, A. V. Afanasjev, G. A. Lalazissis, and P. Ring, *Phys. Rep.* **409**, 101 (2005).
- [24] A. V. Afanasjev and S. Frauendorf, *Phys. Rev. C* **71**, 024308 (2005).
- [25] G. A. Lalazissis, S. Karatzikos, R. Fossion, D. P. Arteaga, A. V. Afanasjev, and P. Ring, *Phys. Lett. B* **671**, 36 (2009).
- [26] U. C. Perera and A. V. Afanasjev, *Phys. Rev. C* **106**, 024321 (2022).
- [27] W. Bertozzi, J. Friar, J. Heisenberg, and J. W. Negele, *Phys. Lett. B* **41**, 408 (1972).
- [28] M. Nishimura and D. W. L. Sprung, *Prog. Theor. Phys.* **77**, 781 (1987).
- [29] C. J. Horowitz and J. Piekarewicz, *Phys. Rev. C* **86**, 045503 (2012).
- [30] H. Kurasawa and T. Suzuki, *Prog. Th. Exp. Phys.* , 113D01 (2019).
- [31] P.-G. Reinhard and W. Nazarewicz, *Phys. Rev. C* **103**, 054310 (2021).
- [32] S. G. Nilsson and I. Ragnarsson, *Shapes and shells in nuclear structure*, (Cambridge University Press, 1995).
- [33] L. Bonneau, P. Quentin, and P. Möller, *Phys. Rev. C* **76**, 024320 (2007).
- [34] G. Coló, H. Sagawa, and P. F. Bortignon, *Phys. Rev. C* **82**, 064307 (2010).
- [35] A. V. Afanasjev and S. Shawaqfeh, *Phys. Lett. B* **706**, 177 (2011).
- [36] J. Dobaczewski, A. V. Afanasjev, M. Bender, L. M. Robledo, and Y. Shi, *Nucl. Phys. A* **944**, 388 (2015).
- [37] A. V. Afanasjev and E. Litvinova, *Phys. Rev. C* **92**, 044317 (2015).
- [38] G. Hagen, M. Hjorth-Jensen, G. R. Jansen, R. Machleidt, and T. Papenbrock, *Phys. Rev. Lett.* **108**, 242501 (2012).
- [39] G. R. Jansen, M. D. Schuster, A. Signoracci, G. Hagen, and P. Navrátil, *Phys. Rev. C* **94**, 011301 (2016).
- [40] G. R. Jansen, J. Engel, G. Hagen, P. Navrátil, and A. Signoracci, *Phys. Rev. Lett.* **113**, 142502 (2014).
- [41] S. K. Bogner, H. Hergert, J. D. Holt, A. Schwenk, S. Binder, A. Calci, J. Langhammer, and R. Roth, *Phys. Rev. Lett.* **113**, 142501 (2014).
- [42] L. B. Karlsson, I. Ragnarsson, and S. Åberg, *Nucl. Phys. A* **639**, 654 (1998).
- [43] E. Caurier, K. Langanke, G. Martínez-Pinedo, F. Nowacki, and P. Vogel, *Phys. Lett. B* **522**, 240 (2001).
- [44] M. Bhuyan, B. Maheshwari, H. A. Kassim, N. Yusuf, S. K. Patra, B. V. Carlson, and P. D. Stevenson, *J. Phys. G* **48**, 075105 (2021).
- [45] P. Navrátil, S. Quaglioni, I. Stetcu, and B. R. Barrett, *Jour. Phys. G* **36**, 083101 (2009).
- [46] B. R. Barrett, P. Navrátil, and J. P. Vary, *Prog. Part. Nucl. Phys.* **69**, 131 (2013).
- [47] F. A. Gareev, S. P. Ivanova, V. G. Soloviev, and S. I. Fedotov, *Phys. Elem. Part. and At. Nucl.* **4**, 357 (1973).
- [48] B. A. Alikov, K. N. Badalov, V. O. Nesterenko, A. V. Sushkov, and J. Wawryszczuk, *Z. Phys. A* **331**, 265 (1988).
- [49] N. Y. Shirikova, A. V. Sushkov, L. A. Malov, and R. V. Jolos, *Eur. Phys. J. A* **51**, 21 (2015).
- [50] E. Litvinova and P. Ring, *Phys. Rev. C* **73**, 044328 (2006).
- [51] E. V. Litvinova and A. V. Afanasjev, *Phys. Rev. C* **84**, 014305 (2011).
- [52] A. K. Jain, R. K. Sheline, P. C. Sood, and K. Jain, *Rev. Mod. Phys.* **62**, 393 (1990).
- [53] J. P. Boisson, R. Piepenbring, and W. Ogle, *Phys. Rep.* **26**, 99 (1976).
- [54] D. Nosek, J. Kvasil, R. K. Sheline, P. C. Sood, and J. Noskova, *Int. J. Mod. Ph. E* **3**, 967 (1994).
- [55] M. K. Balodis, P. T. Prokofjev, N. D. Kramer, L. I. Simonova, K. Schreckenbach, W. F. Davidson, J. A. Pinston, P. Hungerford, H. H. Schmidt, H. J. Scheerer, T. von Egidy, P. H. M. van Assche, A. M. J. Spits, R. F. Casten, W. R. Kane, D. D. Warner, and J. Kern, *Nucl. Phys. A* **472**, 445 (1987).

- [56] T. V. Guseva, A. V. Afanasjev, J. J. Tambergs, and M. K. Balodis, *Bull. Acad. Sc. USSR (ser.phys.)* **51**, 17 (1987).
- [57] M. K. Balodis, N. D. Kramer, P. T. Prokofjev, A. V. Afanasjev, T. V. Guseva, J. J. Tambergs, K. Schreckenbach, W. F. Davidson, D. D. Warner, J. A. Pinston, P. H. M. van Assche, and A. M. J. Spits, *Nucl. Phys. A* **523**, 261 (1991).